Scanning Range Expansion of Planar Phased Arrays using Metasurfaces

Link:
Link to publication record in Heriot-Watt Research Portal

Document Version:
Peer reviewed version

Published In:
IEEE Transactions on Antennas and Propagation

Scanning Range Expansion of Planar Phased Arrays using Metasurfaces

Yan-He Lv, Xiao Ding, *Member*, *IEEE*, Bing-Zhong Wang, *Senior Member*, *IEEE*, and

Dimitris E. Anagnostou, *Senior Member*, *IEEE*

Abstract—We propose a novel method to extend the scanning range of planar phased arrays based on a phase gradient metasurface. The phase gradient metasurface is developed by the generalized Snell's law, which can irregularly tailor the direction of propagation of the traversing electromagnetic waves. The proposed transmission gradient phase metasurface (TGPMS) realizes bidirectional expansion of the scanning range in a phased array application. The TGPMS consists of periodic and multilayer subwavelength elements that contribute to a wide range of transmission phase shift and multiple incident angular stability. The design is verified experimentally with a compact microstrip phased array that is integrated with the proposed TGPMS. Results demonstrate that the TGPMS extends the scanning range of the integrated array symmetrically, from [-36°, 38°] to [-56°, 60°]. The proposed TGPMS has additional desirable characteristics, such as high transmission, polarization insensitivity, tunable transmission phases in a wide range, and transmission phase stability for waves incident at different angles.

Index Terms—Phased array, wide-angle scanning, metasurface, wavefront phase regulation.

I. INTRODUCTION

How to extend the scanning range and how to maintain high quality wide-angle scanning performance are vital challenges in the research field of phased arrays [1]-[2]. In [3], Toshev proposed a multipanel concept to realize wide-angle scanning. This method, which is similar to the combination of mechanical and phase scanning, can extend the scanning range at the cost of impedance mismatch and time. Later, phased arrays consisting of wide-beam or joint wide-beam elements have been reported to hold the potential to achieve wide-angle scanning [4-9]. Typically, joint wide-beam requires the use of reconfigurability techniques.

Recently, several novel approaches for wide-angle scanning have been proposed. Some methods improve the radiation source (electric current source, magnetic current source), while others use switched beams, mechanical adjustments and/or other reconfigurable methods. In addition, some researchers have replaced the metal ground of the current source with the artificial magnetic conductors (AMC), which causes an image source in the same direction to widen the radiation beam and extends the scanning range [10]. Examples that achieve surface wave and sidelobe level reduction include the mutual coupling matching network method [11], tightly coupled arrays [12], hybrid high-impedance surfaces [13], patch mode theory [14], and others. Other efficient methods to improve the scanning performance include

sparse phased arrays [15], the split aperture decoupling technique [16] and higher-order mode excitation for grating lobe reduction [17].

In solving the electromagnetic problem of wide-angle scanning, the aforementioned methods revolve around *boundary conditions*, *Eigen analysis* and *transmission line theory,* which restrict design flexibility. Moreover, in many applications, the antenna platform (and its boundary conditions) and the radiation source (antenna element) are fixed and cannot be altered. New mechanisms to extend the phased array scanning range are desired. This work proposes an innovative method that uses the generalized Snell's law and a transmissive metasurface.

As a two-dimensional metamaterial form, metasurfaces possess unique electromagnetic properties [18-25] as well as ultra-thin structural advantages. Therefore, metasurfaces are widely researched and applied in propagation regulation [26], polarization manipulation [27], dispersion operation [28], impedance matching [29], and energy distribution [30]. Some novel metasurfaces have been designed as impedance matching layers or radomes to improve the performance of phased arrays [31-34]. Besides, the phase gradient technique is one of the most commonly utilized techniques for wave propagation control with metasurfaces [35-41]. Especially for transmissive applications, phase gradient metasurfaces [42-48] are designed with antennas to realize beam steering.

According to the generalized Snell's law, the discontinuous boundary (such as one generated by a phase gradient metasurface) can deflect incident beams to the desired refraction angle. In this paper, a passive transmission gradient phase metasurface (TGPMS) has been developed. The metasurface regulates and manipulates the radiated field and extends the scanning angle range of a phased array. However, symmetrical expansion of the scanning range of the phased array requires the phase distribution of both positive and negative (dual) phase gradients. The proposed TGPMS has high transmission amplitude, a dual-gradient phase distribution, and consists of *multi-layer* subwavelength elements. The metasurface element has a wide range of transmission phases that cover 360°. Moreover, the transmissive phase of metasurface elements is quite stable for waves incident at different angles.

To demonstrate the performance of this novel method, a prototype of the TGPMS is fabricated and integrated with a microstrip phased array operating at 10.3GHz. The experimental realization of the proposed method is also performed on a TGPMS prototype and a microstrip phased array. The scanning range is extended symmetrically from [-36°, 38°] to [-56°, 60°], which validates that the fabricated TGPMS can effectively improve the scanning range.

II. DESIGN AND ANALYSIS OF THE TGPMS

A. Elements design and simulation

To manipulate the phased array radiation by the phase gradient method, the designed TGPMS requires the elements with different transmission phases to construct a gradient distribution. Besides, the proposed TGPMS should have the ability to maintain high transmittance, and high polarization insensitivity. Hence, we chose two fundamental elements with circle patches and square rings, respectively, for estimating the optimal model of the TGPMS element. The structure diagrams and equivalent circuit models of the two

fundamental elements are shown in Figs. 1 (a) and 2 (a), respectively. The structural symmetry of both two types of elements leads to a natural polarization insensitivity. Furthermore, the top and bottom layers of elements have the same metal patterns for enhancing the magnetic coupling.

By means of CST Microwave Studio, two kinds of elements are simulated with varying structural parameters for transmission phase and the magnitude, as shown in Figs. 1(b), 1(c), 2(b) and 2(c). Both two elements are placed in a periodic boundary in x- and y-directions and excited by a waveguide port in z-direction. In Fig. 1(b), square ring elements maintain a high transmittance under the change of the ring widths. Moreover, the operating bandwidth can reach $T_1 = 4.88$ GHz and $T_2 = 8.24$ GHz with transmittance of all curves above 0.8 and 0.9. On the other hand, as shown in Fig. 1(c), the transmission phase of the square ring elements is stable as the variation ranges are only $\phi_1 = 48.2°$ and $\phi_2 = 40.4°$ at 10 GHz and 15 GHz, respectively. These two narrow ranges of phase variation make it difficult to establish a suitable phase gradient boundary on the TGPMS. According to the equivalent circuit model in Fig. 1(a), double-layered metal square ring is inductive in the transmission matrix, while the coupled thin dielectric layer can be equivalent to a short transmission line, which is connected in series with a characteristic impedance $Z_a = Z_0 / \sqrt{\varepsilon_r}$. Z_0 is the wave impedance in free space. From another point of view, the width variation of the double-layered square ring changes the equivalent inductance of the inductive network above, which produces a small range of transmissive phase shifts and a common wideband of high transmission magnitude.

For elements with circular patches, the ranges of phase variation can reach to $\phi_3 = 113.2°$ and $\phi_4 = 324.1°$ at the same frequencies as before, as shown in Fig. 2(b). However, the bandwidth with transmittance higher than 0.7 only reaches $T_3 = 1.47$GHz when the element has circular patches, as shown in Fig. 2(c). It is noted that the equivalent circuit model in Fig. 2(a) indicates the capacitive transmission matrix, which means that the radius variation of a circular patch manipulates the equivalent capacitance changes between two open parts in the free space. Therefore, the sensitive phase shift and a common narrow band with high transmission magnitude are both caused by the equivalent capacitance variation of a capacitive transmission matrix. Based on this analysis, the element with square rings has a high transmittance, while the circular patch elements possess a wide range of transmission phases. Hence, the TGPMS element can be evolved by the combination of these two elements, as shown in Fig. 3(a). In a two-port transmission line network, the combination of two fundamental elements can integrate capacitive and inductive equivalent circuit models into one transmission matrix, as shown in Fig. 3(b). Besides, the geometric parameters of TGPMS elements are fine-tuned for both wide range of transmission phase, and high transmittance over a broad range of frequencies. The above combined element structure is also applied to the metasurface with the phase compensation principle, which can improve the radiation characteristics of the antenna [36].

Finally, the proposed element is based on a classic sandwich structure, where the top and bottom layers are homocentric combinations of square ring and circular patches. The mid substrate has dielectric constant $\varepsilon_r = 2.6$ and thickness $d = 1.4$ mm. The square ring has outer diameter the same as the period $p = 10$ mm and width $w = 0.2$ mm. When the radius r of the circular patch is adjusted from 2 to 4.6 mm, the transmission amplitude and the transmission phase are simulated, shown as in Figs. 3(c) and 3(d), respectively. According to Figs. 3(c) and 3(d), the elements can acquire transmissive phase ranges of 240.4° and 367° at the frequencies of 9.3
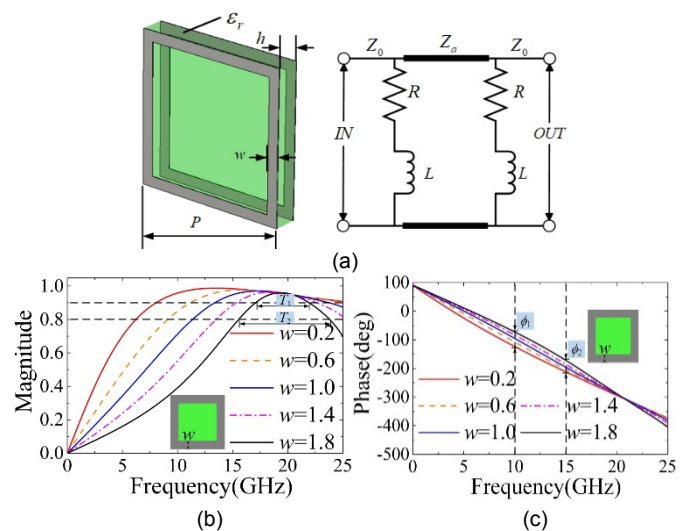

Fig. 1. (a) Schematics and equivalent circuit models of the square ring element. (b) Transmission magnitude with $w = 0.2$, 0.6, 1.0, 1.4 and 1.8mm. The bandwidth of all curves with magnitude greater than 0.9 and 0.8 are T_1 and T_2, respectively. (c) Transmission phase with $w = 0.2$, 0.6, 1.0, 1.4 and 1.8mm. The phase variation ranges at 10 GHz and 15 GHz are ϕ_1 and ϕ_2, respectively.
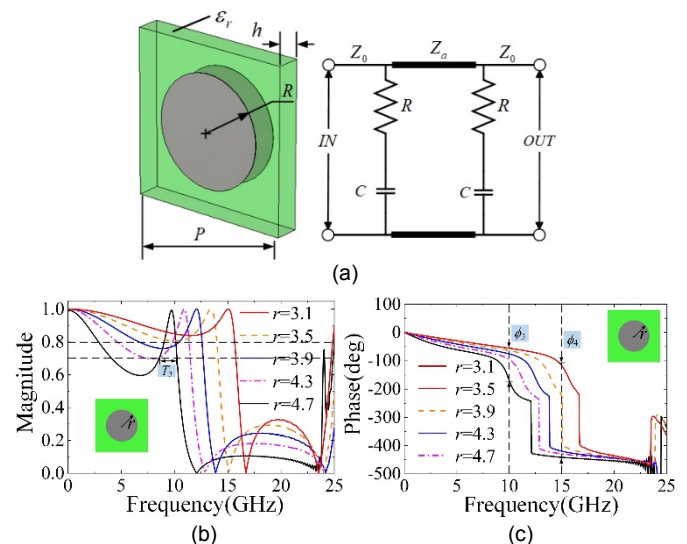

Fig. 2. (a) Schematics and equivalent circuit models of the circular patch elements. (b) Transmission magnitude with $r = 3.1$, 3.5, 3.9, 4.3 and 4.7mm. The bandwidth of all curves with magnitude greater than 0.7 is T_3. (c) Transmission phase with $r = 3.1$, 3.5, 3.9, 4.3 and 4.7mm. The phase variation ranges at 10 GHz and 15 GHz are ϕ_3 and ϕ_4 , respectively.

GHz and 10.3 GHz, respectively, as well as a broad bandwidth of 1.13 GHz with the transmittance higher than 0.8, which fully satisfies the requirements of TGPMS for broad phase range and high transmittance.

As mentioned earlier, another challenge for the TGPMS element is to be stable to the incident angles of waves. The main lobe of the phased array is scanned within a symmetrical range as the progressive phase shift changes. Therefore, the proposed TGPMS element needs to have a stable transmission phase for multiple incident angles. In this paper, a method of increasing the number of layers is employed to stabilize the transmission phase of multi-angle incident waves. In Fig. 4(a), we compare the simulated transmission phase curves of the elements with layers $g = 1$, 2, 3, 4 at incident wave angles 0°, 10°, 20°, 30°, and 40° (20 cases in total). By comparing all the curves, the
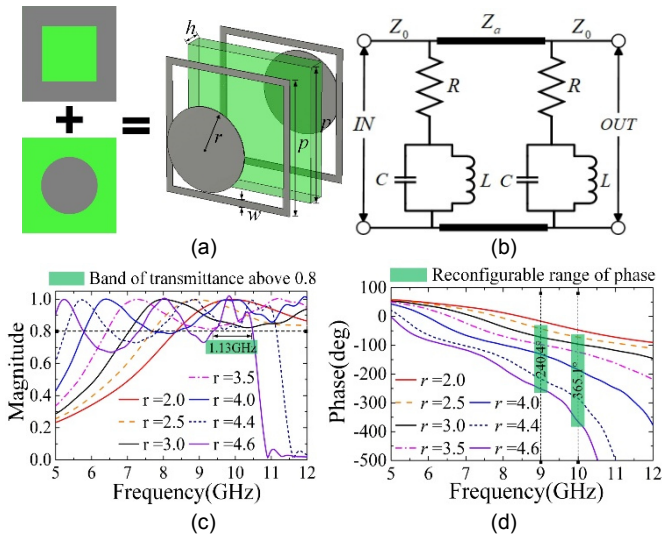
(a) (b)

(c) (d)

Fig. 3. (a) Evolution process, structural configuration and the (b) equivalent circuit model of the TGPMS element. (c) Simulated transmission magnitude and (d) transmission phase of the TGPMS element with $r = 2, 2.5, 3, 3.5, 4, 4.4$ and 4.6 mm. The high transmittance bandwidth of all curves with magnitude greater than 0.8 is 1.13 GHz. The phase variation ranges are 240.4° and 365.1° at 9 GHz and 10 GHz, respectively.
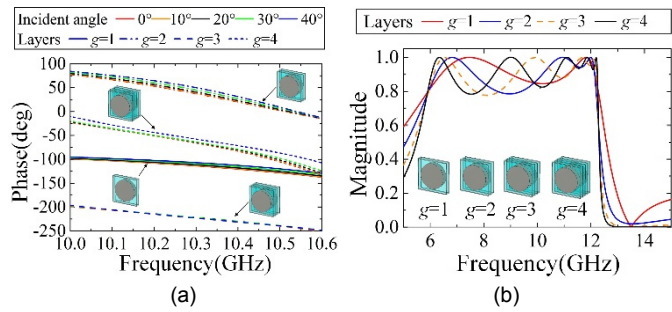

(a) (b)

Fig. 4. Transmission phase stability of TGPMS elements for multiple incident angles and the influences of multilayer structure on transmittance (a) The transmission phase of incident beams at different angles of 0º, 10º, 20º, 30º and 40º for TGPMS elements with different layers $g=1, 2, 3, 4$ at 10.3 GHz. (b) The transmission magnitude of TGPMS elements with different layers $g=1, 2, 3, 4$.

elements with $g = 1, 2, 3, 4$ layers have different transmission phases at multiple incident angles, therefore, four separate strip areas are indicated on the chart of Fig. 4(a). The width of the four strip areas is proportional to the stability of the transmission phase of the TGPMS with different layers under the incident angle changing from 0° to 40°. However, for the TGPMS elements, the increase in the number of layers also means increased electromagnetic losses and decreased transmittance. Fig. 4(b) presents the transmission magnitude curves of the elements, so that the simulation results can indicate the electromagnetic loss and the transmittance with different layers $g = 1, 2, 3, 4$. The element with $g = 3$ has the narrowest strip region (Fig. 4(a)) and the highest transmittance (Fig. 4(b)) at 10.3 GHz.

Consequently, the optimal TGPMS element is designed using $g = 3$ layers that achieve high transmittance and efficient insensitivity of the transmissive phases to waves of different incident angles.

B. Operation principle based on the generalized Snell's law

In order to extend symmetrically the scanning range of the phased array, a high transmittance boundary with discontinuous phases of the dual-gradient distribution should be designed and set above the radiation aperture, which operates in accordance with the generalized Snell's law [35].
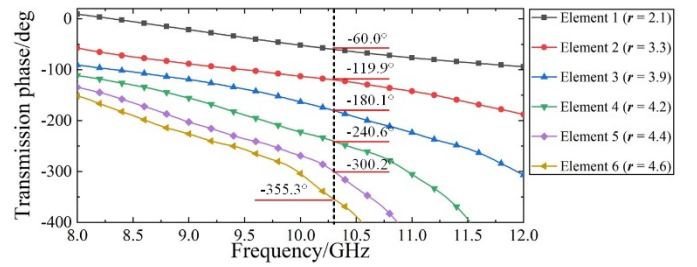

Fig. 5. Transmission phase of six different elements in a period of the proposed metasurface, which have circular patches with different radius. Moreover, the transmission phases of six different elements change from -60.0° to -355.3° with approximately 60° spacing at 10.3 GHz.
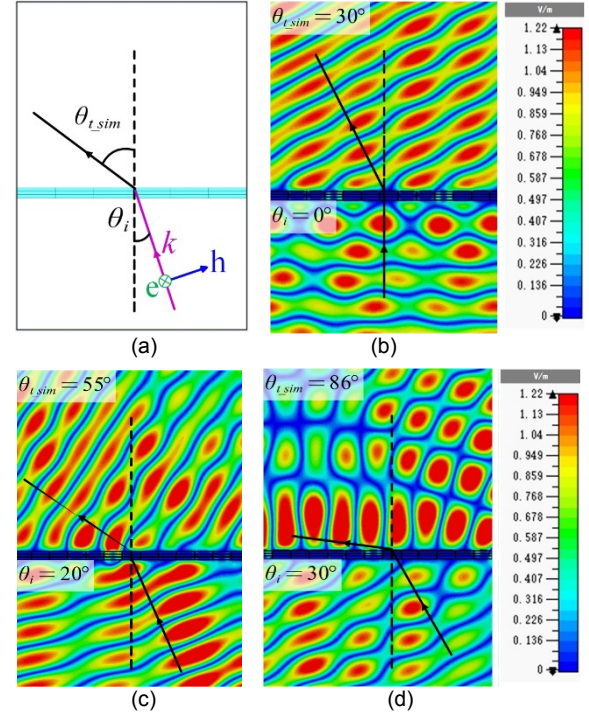

(a) (b)

(c) (d)

Fig. 6 (a) Schematic of plane wave incident on the metasurface sequence at angle θ_i. The electric field distribution of the proposed metasurface when it is illuminated by the plane wave of incident angle θ_i = (b) 0°, (c) 20° (d) and 30°

To verify the beam deflection performance of the TGPMS, a transmissive metasurface with a phase gradient distribution in the y-direction is simulated using the commercial software CST Microwave Studio. To simulate the beam deflection effect, an MS sequence is surrounded by a periodic boundary to be equivalent to an infinite phase gradient boundary. Two ports are set in the z direction for transmitting and receiving, respectively. A period of the metasurface sequence consists of six proposed units with different geometric parameters, which generate the transmission phase response of -360°, -300°, -240°, -180°, -120°, and -60° on Elements 1 ~ 6, respectively, as shown in Fig. 5. The above simulation results can also demonstrate that the structure-parameter variation of the proposed three-layer combined unit cell realizes a common band of high transmission amplitude, a wide range of transmission phase shift, and a periodic sequence of transmission phases with a step of 60°. For the expected objective of this paper, this appropriate result can also be strongly verified by the design method of transmission array cells [49-52]. When it comes to the operation principle, the design method of the TGPMS in this paper is different from that of the transmitarray antenna. For a transmitarray antenna, the required phase shift for each element depends on the phase delay between the incident wave and the expected transmission wave.

This design process is similar to achieve the focusing or spherical-plane wave conversion by a transmissive metasurface, which is based on the phase compensation principle. However, the required transmission phase of each unit cell on the TGPMS in this paper is calculated from the required phase gradient and the period. This is an effective means to realize beam deflection based on the generalized Snell's law. In addition, the main differences between our design and a transmitarray are also on the unit cell size and the application of phase gradient to extend the scanning range.

To verify the above analysis, a 1D MS sequence of four periods is simulated for electric field distribution under incident plane waves at the angle $\theta_i = 0°$, $20°$ and $30°$ mentioned above. The designed metasurface is illuminated by X-polarized plane waves with incident angles $\theta_t = 0°$, $20°$ and $30°$. The ideal refraction angles θ_{t_ide} from the present metasurface can be calculated by the generalized Snell's law [34]:

$$\sin(\theta_t)n_t - \sin(\theta_i)n_i = \frac{\lambda_o}{2\pi}\frac{\Delta\phi}{\Delta x} \tag{1}$$

$$\theta_{t\_ide} = \arcsin\left(\frac{\pi}{3}\frac{\lambda_o}{2\pi}\frac{1}{p} + \sin(\theta_i)\right) \tag{2}$$

Eq. (1) is the general expression for generating an arbitrary refraction angle by the generalized Snell's law, where n_i and n_t are the refractive indices of the incident media and the refractive media, respectively. Moreover, the phase change $\Delta\phi$ and the periodicity of the proposed elements in Fig. 5 are $60°$ and $p = 10$ mm, respectively. When the beam passes through a metasurface with negligible thickness in free space, there should be $n_t = n_i = 1$. Therefore, Eq. (2) for θ_t, which represents the refraction angle obtained by the plane wave entering the designed MS at an angle θ_i, can be simplified. When the incident angles are $\theta_i = 0°$, $20°$ and $30°$, the ideal refraction angles θ_{t_ide} are about $29.69°$, $54.83°$ and $84.27°$, respectively.

According to the electric field distribution in Fig. 6, the observed simulation results of the refraction angles θ_{t_sim} are about $30°$, $55°$ and $86°$, which are very close to the ideal results calculated by (2). The above simulations demonstrate that the proposed TGPMS consisting of six element phase status can realize precise beam manipulation for plane waves. This provides technical support for extending the phased array scan range based on TGPMS.

C. Metasurface design

To verify the proposed TGPMS, a multi-layer phase gradient MS consisting of the above transmissive elements was loaded onto a microstrip phased array operating at 10.3 GHz, which were processed together for experiments. Considering the element characteristics above and the symmetry of the radiation, the proposed TGPMS should be developed with both three-layer structure and dual gradient phase distribution. This would allow the phased array to symmetrically modulate the radiation beams and extend its scanning range. The TGPMS consists of the elements with different transmission phases, which are determined by the generalized Snell's law, and form a phase gradient boundary on the metasurface. Furthermore, a construction equation of the TGPMS can be obtained from the generalized Snell's law:

$$\alpha = 2\pi N(\sin\theta - \sin\theta_i) \tag{3a}$$

$$N = (p \cdot f) / c \tag{3b}$$

$$\alpha = 2\pi N(\sin\theta_{MS} - \sin\theta_{PAA}) + K \tag{3c}$$

$$K\begin{cases} = 0.5 & \theta_{PAA} \in [15°, 40°] \cup [-40°, -15°] \\ = 0.57 & \theta_{PAA} \in [3°, 15°] \cup [-15°, -3°] \end{cases} \tag{3d}$$
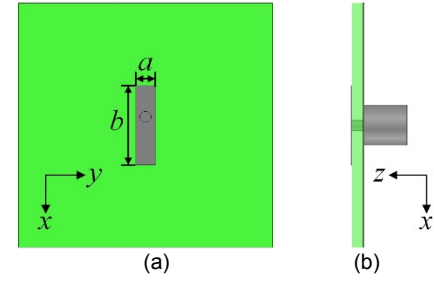

Fig. 7 Schematic layout of the fundamental microstrip antenna element of the phased array. (a) Top view. (b) Side view.
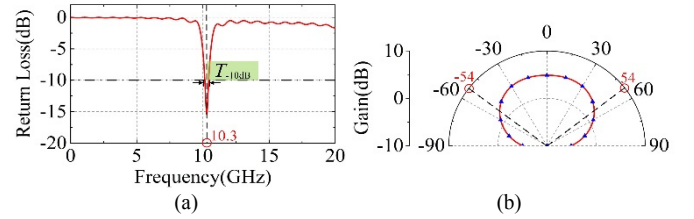
Fig. 8 Simulation results of the fundamental microstrip antenna element of the phased array. (a) Reflection coefficient. (b) Radiation pattern.
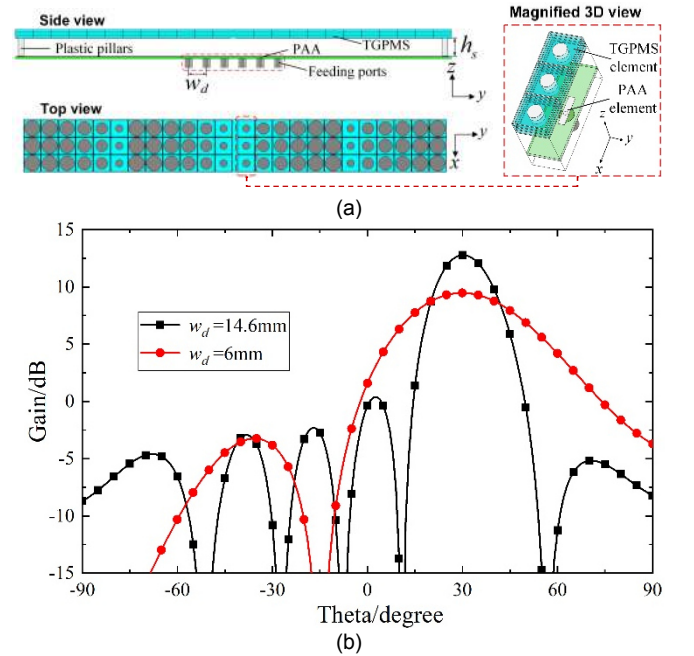
Fig. 9 (a) Structure diagram with the configuration of the TGPMS integrated with the phased array antenna (PAA), along with a 3D magnified schematic. (b) Patterns of the PAA with element spacing $w_d = 6$ and 14.6 mm (0.5 λ) when the main lobe direction is 30°.

where, α is the phase step between elements, p is the period of the element, and f is the operating frequency. Based on the original and the desired scanning range, the initial value of the phase gradient required by TGPMS is calculated by Eq. (3a). However, due to the limitations of beamwidth, gain fluctuations, port coupling, and electromagnetic losses in practical application scenarios, the required phase gradient needs a compensation, as shown in Eq. (3c). Among them, K is determined through multiple simulation results.

Further to the design of the TGPMS, a compact microstrip phased array with 6 elements is developed for this experimental demonstration. The main element of the phased array is a microstrip antenna with width $a = 2$ mm and length $b = 8.8$ mm as shown in Figs. 7(a) and (b). By means of the CST Microwave Studio, the radiation performance of the antenna has been analyzed and is shown in Figs.

8(a) and (b). The antenna element has efficient radiation at 10.3 GHz, as well as an operating band of T_{-10dB} = 310 MHz (see Fig. 8(a)). Besides, the 3-dB beamwidth of the antenna can reach $\pm 54^\circ$ as seen in the radiation pattern of Fig. 8(b).

Based on this microstrip element, the phased array prototype is developed and integrated with the TGPMS. In Fig. 9(a), a PAA composed of the above antenna element has been loaded with a TGPMS, which is designed as a bidirectional gradient phase distribution with 4×3 periodic sequence. Considering the pattern of the PAA, we require the PAA to have as few sidelobe as possible when the SLL is as low as possible to improve the accuracy of the design method. Therefore, we choose a narrower element spacing wd=6mm to design the PAA which can be calculated by a matrix-factor equation containing the coupling. In Fig. 9(b), PAAs with different element spacing w_d = 6 and 14.6 mm are simulated when the main lobe direction is 30º. Moreover, the effect of the tight arrangement of the array elements on the radiation patterns is discussed again in the subsequent experiments. Fig. 9(a) also shows that the proposed phased array is fixed at h_s = 13.5mm below the TGPMS and is held in place by nylon pillars. We have given a detailed discussion about h_s in the supplementary material. A narrow w_d (w_d = 6mm < 0.5λ) demonstrates that the phased array elements are closely arranged to suppress the gain of high order side lobes, which assists TGPMS to enhance the effect of extending the scanning range.

III. EXPERIMENTAL RESULTS

The prototype of TGPMS and microstrip phased array are fabricated and integrated together at a fine-tuned and optimized distance, as shown in Fig. 10(a). The TGPMS consists of 3 × 24 elements, and the aperture of an entire phased array system occupies a size of 270mm × 60mm. Fig. 10(b) shows the phased array and the TGPMS during performance characterization measurements in the anechoic chamber. The phased array loaded with the TGPMS is connected to a port of a vector network analyzer (VNA) for excitation and fixed onto a rotating platform. The rotating platform has a rotation range from -90º to 90º. A standard horn (8 to 15 GHz) is connected on the other port of the VNA and is placed on a support platform with the same height as the phased array. The rotating platform and the support platform are on the same plane. The phased array without the TGPMS has also been measured for comparison.

In Figs. 11(a)-(h) and in Table I , the far-field radiation patterns of the phased array and of the phased array with the integrated TGPMS are both measured at 10.3 GHz. According to the results, the original scanning range [-36º, 38º] of the phased array has now been extended to a wide range of [-56º, 60º] thanks to the TGPMS. In other words, the designed TGPMS can bi-directionally move the radiation beam of the traditional phased array to a wider angular region.

It is noted that the phased array when it is integrated with the TGPMS has stable gain with very little fluctuation. As mentioned in Section II.C, the spacing between antenna elements of the proposed PAA is narrower than 0.5λ. However, the loading of TGPMS compresses the radiated energy to the desired direction without pattern distortion and gain fluctuation. By means of the TGPMS, the radiated energy is compressed to the desired direction, so the SLL has been greatly improved. Besides, for patterns at different progress phases in Table I, the PAA with TGPMS radiates narrower main beams than the PAA without TGPMS. However, the gain of the PAA with TGPMS becomes lower than that of the PAA without TGPMS. This is due to the electromagnetic loss caused by the three-layer MS.

Subsequently, according to the experimental results, the main lobes of the phased array with and without the TGPMS can be corresponded to the θ_t and θ_i in Eq. (3a), so that an equivalent phase step between elements can be calculated from α_e by the θ_t and θ_i , as shown on
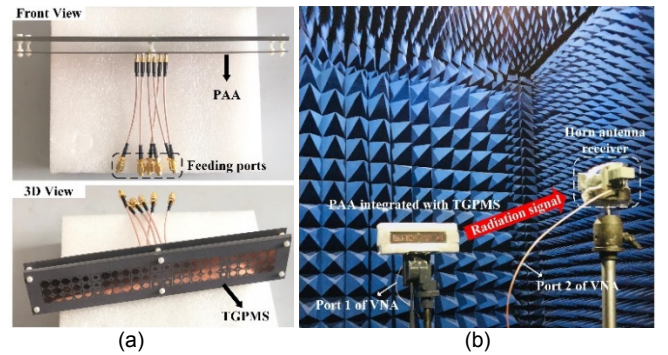
Fig.10. (a) Photos of the front view and 3D view of a prototype of the TGPMS integrated with the phased array. (b) Photo of the measurement setup inside the anechoic chamber.
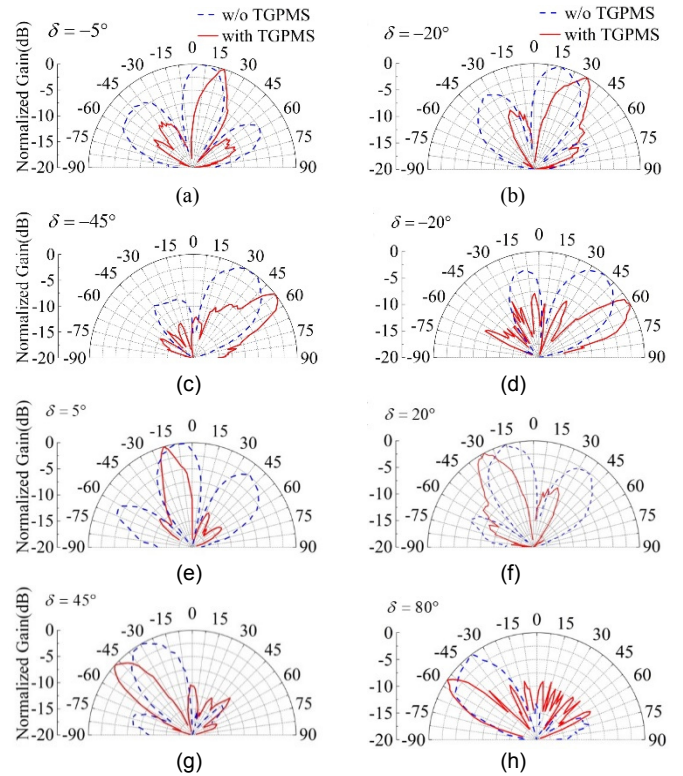
Fig.11. Measured radiation patterns showing the beam scanning of the phased array with and without the TGPMS, when the progressive phase shift δ is (a) -5º, (b) -20º, (c) -45º, (d) -80º, (e) 5º, (f) 20º, (g) 45º, and (h) 80º, respectively.
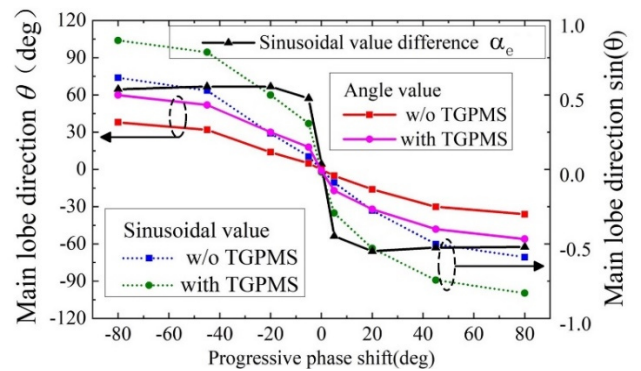
Fig.12. The distribution curve of different α_e values with the progressive phase from -80º to 80º.

TABLE I.   Measured results of Phased Array

Progressive phase shift	Main lobe direction θ		Gain (dBi)		SLL(dB)	
	w/out MS*	with MS*	w/out MS*	with MS*	with MS*	w/out MS*
-80°	38°	60°	9.53	8.93	-7.69	-2.72
-45°	32°	52°	9.59	9.44	-12.87	-7.54
-20°	14°	30°	10.34	9.62	-7.91	-2.68
-5°	5°	18°	10.82	9.73	-9.92	-4.13
0°	0°	-1°	11.23	10.61	-10.18	-4.89
5°	-5°	-17°	10.91	9.57	-13.95	-2.57
20°	-16°	-32°	9.63	9.24	-8.23	-2.65
45°	-30°	-48°	9.54	8.95	-10.73	-7.94
80°	-36°	-56°	9.48	8.29	-8.89	-12.53

* MS is an acronym for metasurface.

TABLE II.   Sinusoidal value of the main lobe direction of Phased Array

Progressive phase shift	Sinusoidal value of the main lobe direction $\sin(\theta)$		α_e	α
	without MS*	with MS*		
-80°	0.616	0.866	0.539	
-45°	0.530	0.788	0.557	0.547
-20°	0.242	0.500	0.556	
-5°	0.087	0.309	0.478	
0°	0	-0.017	0.037	
5°	-0.087	-0.292	-0.447	
20°	-0.275	-0.530	-0.548	-0.547
45°	-0.500	-0.743	-0.524	
80°	-0.588	-0.829	-0.520	

* MS is an acronym for metasurface.

Table II. In Fig. 12, the solid lines in red and magenta color illustrate respectively the main lobe direction angle of the phased array with and without the TGPMS. Moreover, the dashed lines of blue and green color illustrate respectively the sinusoidal value of the main lobe of the phased array with and without the TGPMS. Besides, the solid black line represents the α_e, which tends to two symmetrical horizontal lines for positive and negative progressive phase shifts, respectively. Regardless of the positive or negative progressive phase shifts, the phased array with the TGPMS (red solid line) has a wider scanning range. For all progressive phase shifts, the blue and green dash lines also show the same trend as the red and magenta solid lines, respectively. It is worth noting that the characteristics of each curve are consistent with our working principle of Eq. (3a):

(*a*) when comparing red and magenta lines, the main lobe expansion (solid magenta) of the TGPMS is not uniform for different progressive phase shifts.

(*b*) When comparing green and blue lines, the spacing between the green and blue dashed lines tends to be stable for all progressive phase shifts.

(*c*) All curves in Fig. 12 demonstrate a broadside radiation when the progressive phase shift is 0.

The characteristics in (*a*) and (*b*) above verify the principle of Eq. (3a). Besides, the characteristics in (*c*) are consistent with the discontinuity of the phase gradient at the center of the TGPMS.

IV. Conclusion

This work proposed and validated a new method for extending the scanning angle of planar phased arrays through the TGPMS in this paper, and breaks the bottleneck of their scanning angle limitation. The TGPMS consists of transmissive elements that combines both a high transmission amplitude and a wide range of transmission phases. The experimental implementation based on the presented TGPMS and microstrip phased arrays have also been performed, which eventually extended the scanning range from (-36º, 38º) to (-56º, 60º). Besides, the physical principles of the TGPMS were explained and verified by comparing Eq. (1) with the experimental radiation patterns. The proposed novel approach enables new applications for electromagnetic metamaterials, in the fields of seeker phased arrays, smart skins, and radiation shaping.

References

[1] J. D. Kraus and R. J. Marhefka, *Antennas For All Applications*, 3rd ed., New York, NY, USA: McGraw-Hill, 2003.

[2] R. J. Mailloux, *Phased Array Antenna Handbook* (Artech HouseAntennas and Propagation Library), 2nd ed., Norwood, MA, USA: Artech House, 2008

[3] A. G. Toshev, "Multipanel concept for wide-angle scanning of phased array antennas," *IEEE Trans. Antennas Propag.*, vol. 56, no. 10, pp. 3330-3333, Oct. 2008.

[4] E. B. Lima, S. A. Matos, J. R. Costa, C. A. Fernandes, and N. J. G. Fonseca, "Circular polarization wide-angle beam steering at ka-band by in-plane translation of a plate lens antenna," *IEEE Transactions on Antennas and Propagation*, vol. 63, no. 12, pp. 5443-5455, Dec. 2015.

[5] G. W. Yang, J. Y. Li, D. J. Wei, and R. Xu, "Study on wide-angle scanning linear phased array antenna," *IEEE Trans. Antennas Propag.*, vol. 66, no. 1, pp. 450-455, Jan. 2018.

[6] H. Y. Zhou, A. Pal, A. Mehta, H. Nakano, A. Modigliana, T. Arampatzis, P. Howland, "Reconfigurable phased array antenna consisting of high-gain high-tilt circularly polarized four-arm curl elements for near horizon scanning satellite applications," *IEEE Antenna Wireless Propag. Lett.*, vol. 17, no. 12, pp. 2324-2328, Oct. 2018.

[7] X. Ding, Y.-F. Cheng, W. Shao, H. Li, B.-Z Wang, and D. E. Anagnostou, "A wide-angle scanning planar phased array with pattern reconfigurable magnetic current element," *IEEE Transactions on Antennas and Propag.*, vol. 65, no. 3, pp. 1434-1439, Mar. 2017.

[8] N. Haider, A. G. Yarovoy, and A. G. Roederer, "L/S-band frequency reconfigurable multiscale phased array antenna with wide angle scanning," *IEEE Transactions on Antennas and Propag.*, vol. 65, no. 9, pp. 4519-4528, Sep. 2017.

[9] X. Ding, B.-Z. Wang, and G.-Q. He, "Research on a millimeter-wave phased array with wide-angle scanning performance," *IEEE Trans. Antennas Propag.*, vol. 61, no. 10, pp. 5319-5324, Oct. 2013.

[10] R. Wang, B.-Z. Wang, X. Ding, and X.-S. Yang, "Planar phased array with wide-angle scanning performance based on image theory," *IEEE Trans. Antennas Propag.*, vol. 63, no. 9, pp. 3908–3917, Sep. 2015

[11] B. A. Arand, A. Bazrkar, and A. Zahedi, "Design of a phased array in triangular grid with an efficient matching network and reduced mutual coupling for wide-angle scanning," *IEEE Trans. Antennas Propag.*, vol. 65, no. 6, pp. 2983-2911, June. 2017.

[12] E. Yetisir, N. Ghalichechian, and J. L. Volakis, "Ultrawideband array with 70° scanning using FSS superstrate," *IEEE Trans. Antennas Propag.*, vol. 64, no. 10, pp. 4256-4265, Oct. 2016.

[13] A. Pal, A. Mehta, D. Mirshekar-syahkal, and H. Nakano, "2×2 phased array consisting of square loop antennas for high gain wide angle scanning with low grating lobes," *IEEE Trans. Antennas Propag.*, vol. 65, no. 2, pp. 576-583, Feb. 2017.

[14] X. Ding, Y.-F. Cheng, W. Shao, B.-Z. Wang, "A wide-angle scanning phased array with microstrip patch mode reconfiguration technique," *IEEE Transactions on Antennas and Propag.*, vol. 65, no. 9, pp. 4548-4555, Sep. 2017.

[15] F. F. Manzillo, M. Smierzchalski, L. Le Coq, M. Ettorre, J. Aurinsalo, ´ K. T. Kautio, M. S. Lahti, A. E. Lamminen, J. Saily, and R. Sauleau, "A wide-angle scanning switched-beam antenna system in LTCC technology with high beam crossing levels for V-band communications," *IEEE Transactions on Antennas and Propag.*, vol. 67, no. 1, pp. 541-553, Jan. 2019.

[16] A. Kedar and L. P. Ligthart, "Wide scanning characteristics of sparse phased array antennas using an analytical expression for directivity," *IEEE Transactions on Antennas and Propag.*, vol. 67, no. 2, pp. 905-974, Feb. 2019.

[17] Z. lqbal and M. pour, "Grating lobe reduction in scanning phased array antennas with large element spacing," *IEEE Transactions on Antennas and Propag.*, vol. 66, no. 12, pp. 6965-6974, Dec. 2018.

[18] G. Moreno, A. B. Yakovlev, H. M. Bernety, D. H. Werner, H. Xin, A. Monti, F. Bilotti, A. Alù, "Wideband elliptical metasurface cloaks in printed antenna Technology," *IEEE Transactions on Antennas and Propag.*, vol. 66, no. 7, pp. 3512-3525, Apr. 2018.

[19] N. M. Estakhri, and A. Alù, Ultra-thin unidirectional carpet cloak and wavefront reconstruction with graded metasurfaces. *IEEE Antennas Wireless Propag. Lett.*, vol. 13, pp. 1775-1778, Nov. 2014.

[20] G. V. Eleftheriades, A. K. Iyer, P. C. Kremer, "Planar negative refractive index media using periodically LC loaded transmission lines," *IEEE transactions on Microwave Theory and Techniques,* vol. 50, no. 12, pp. 2702-2712, Dec. 2002.

[21] A. K. Lyer, and G. V. Eleftheriades, "A multilayer negative-refractive-index transmission-line (NRI-TL) metamaterial free-space lens at X-band," *IEEE Trans. Antennas Propag.*, vol. 55, no. 10, pp. 2746-2753, Oct. 2007.

[22] A. Epstein, and G. V. Eleftheriades, "Passive lossless Huygens metasurfaces for conversion of arbitrary source field to directive radiation," *IEEE Trans. Antennas Propag.*, vol. 62, no. 11, pp. 5680-5695, Nov. 2014.

[23] T. Nakamura and T. Fukusako, "Broadband design of circularly polarized microstrip patch antenna using artificial ground structure with rectangular unit cells," *IEEE Trans. Antennas Propag.*, vol. 59, no. 6, pp. 2103–2010, Jun. 2011.

[24] Y. Shang, and Z. X. Shen, "Polarization-Independent Backscattering Enhancement of Cylinders Based on Conformal Gradient Metasurfaces," *IEEE Trans. Antennas Propag.*, vol. 65, no. 5, pp. 2386–2396, May. 2017.

[25] O. Quevedo-Teruel, M. Ebrahimpouri, and M. Ng Mou Kehn, "Ultra wide band metasurface lenses based on off-shifted opposite layers," *IEEE Antennas Wireless Propag. Lett.*, vol. 15, pp. 484–487, 2016.

[26] O. Manoochehri, A. Darvazehban, M. A. Salari, A.Emadeddin, and D. Erricolo, "A Parallel Plate Ultrawideband Multibeam Microwave Lens Antenna" *IEEE Trans. Antennas Propag.*, vol. 66, no. 9, pp. 4878-4883, Jun. 2018.

[27] X. X. Liu, Y. Zhao, and A. Alù, "Polarizability tensor retrieval for subwavelength particles of arbitrary shape," *IEEE Trans. Antennas Propag.*, vol. 64, no. 6, pp. 2301-2310, Mar. 2016.

[28] K. Achouri, A. Yahyaoui, S. Gupta, H. Rmili, and C. Caloz, "Dielectric resonator metasurface for dispersion engineering," *IEEE Trans. Antennas Propag.*, vol. 65, no. 2, pp. 673-680, Nov. 2016.

[29] A. H. Dorrah, M. Chen, G. V. Eleftheriades, "Bianisotropic Huygens' metasurface for wideband impedance matching between two dielectric media," *IEEE Trans. Antennas Propag.*, vol.66, no. 9, pp. 4729-4742, Jun. 2018.

[30] M. Silveirinha, and N. Engheta, "Tunneling of electromagnetic energy through subwavelength channels and bends using ε-near-zero materials," *Physical review Lett.*, vol. 97, no. 15, 157403, Oct. 2006.

[31] S. Sajuyigbe, M. Ross, P. Geren, S. A. Cummer, M. H. Tanielian, and D. R. Smith, "Wide angle impedance matching metamaterials for waveguide-fed phased-array antenna," *IET Microw., Antennas, Propagat.*, vol. 4, pp. 1063–1072, 2010

[32] T. R. Cameron and G. V. Eleftheriades, "Analysis and characterization of a wide-angle impedance matching metasurface for dipole phased arrays," *IEEE Trans. Antennas Propag.*, vol. 63, no. 9, pp. 3928–3938, Sep. 2015.

[33] A. O. Bah, P.-Y. Qin, R. W. Ziolkowski, Q. Cheng, and Y. J. Guo, "Realization of an ultra-thin metasurface to facilitate wide bandwidth, wide angle beam scanning," *Sci. Rep.*, vol. 8, no. 1, Mar. 2018, Art. no. 4761.

[34] A. Benini, E. Martini, S. Monni, M. C. Vigano, F. Silvestri, E. Gandini, G. Gerini, G. Toso, S. Maci., "Phase-gradient meta-dome for increasing gratinglobe-free scan range in phased arrays," *IEEE Trans. Antennas Propag.*, vol. 66, no. 8, pp. 3973–3982, Aug. 2018.

[35] N. Yu, P. Genevet, M. A. Kats, F. Aieta, J. P Tetienne, F. Capasso, and Z. Gaburro, "Light propagation with phase discontinuities: generalized laws of reflection and refraction," Science, 1210713, Sep. 2011.

[36] H. Li, G. M. Wang, H.-X. Xu, T. Cai, and J. Liang, "X-band phasegradient metasurface for high-gain lens antenna application," *IEEE Trans. Antennas Propag.*, vol. 63, no. 11, pp. 5144–5149, Nov. 2015.

[37] T. Cai, G. Wang, X. Zhang, J. Liang, Y. Zhuang, D. Liu, and H. Xu, "Ultra-thin polarization beam splitter using 2-D transmissive phase gradient metasurface," *IEEE Trans. Antennas Propag.*, vol. 63, no. 12, pp. 5629–5636, Dec. 2015.

[38] H. Li, G. Wang, J. Liang, X. Gao, H. Hou, and X. Jia, "Single-layer focusing gradient metasurface for ultrathin planar lens antenna application," *IEEE Trans. Antennas Propag.*, vol. 65, no. 3, pp. 1452–1457, Mar. 2017.

[39] X. Wan, L. Zhang, S. L. Jia, J. Y. Yin, and T. J. Cui, "Horn antenna with reconfigurable beam-refraction and polarization based on anisotropic Huygens metasurface," *IEEE Trans. Antennas Propag.*, vol. 65, no. 9, pp. 4427–4434, Sep. 2017.

[40] E. Erfani, M. Niroo-Jazi, and S. Tatu, "A high-gain broadband gradient refractive index metasurface lens antenna," *IEEE Trans. Antennas Propag.*, vol. 64, no. 5, pp. 1968–1973, May 2016.

[41] A. Dadgarpour, B. Zarghooni, B. S. Virdee, and T. A. Denidni, "Beam deflection using gradient refractive-index media for 60-GHz end-fire antenna," *IEEE Trans. Antennas Propag.*, vol. 63, no. 8, pp. 3768–3774, Aug. 2015.

[42] H. F. Ma, X. Chen, X. M. Yang, W. X. Jiang, and T. J. Cui, "Design of multibeam scanning antennas with high gains and low sidelobes using gradient-index metamaterials," *J. Appl. Phys.*, vol. 107, pp. 114902, Jan. 2010.

[43] Y. H. Liu, C. C. Liu, X. Y. Jin, B. Y. Zhang, Y. H. Zhang, X. Q. Zhu, B. Su, and X. P. Zhao, "Beam steering by using a gradient refractive index metamaterial planar lens and a gradient phase metasurface planar lens," *Microw. Opt. Technol. Lett*, no. 60, vol. 2, pp. 330-337, Jan. 2018.

[44] B. Ratni, J. Yi, X. Ding, A. de Lustrac, K. Zhang, G.-P. Piau, and S. N. Burokur, "Gradient phase partially reflecting surfaces for beam steering in microwave antennas," *Opt. Exp.*, vol. 26, no. 6, pp. 6724-6738, 2018.

[45] W. Li, S. Xia, Z. Li, Z. Xu, L. Li, H. Shi and A. Zhang, "PIN tuned phased-gradient-metasurface transmittarray for beam steering application," *11th Intern. Symp. Antennas Propag. EM Theory (ISAPE)*, pp. 276-278, Guilin, China, 2016.

[46] J. J. Liang, G. L. Huang, J. N. Zhao, Z. J. Gao, and T. Yuan, "Wideband Phase-Gradient Metasurface Antenna With Focused Beams," *IEEE Access*, vol. 7, pp. 20767-20772, May, 2019.

[47] K. K. Katare, A. Biswas, and M. J. Akhtar, "Microwave beam steering of planar antennas by hybrid phase gradient metasurface structure under spherical wave illumination," *J. Appl. Phys.*, vol. 122, no. 23, pp. 234901, Dec. 2017.

[48] Y. Liu, J. Fu, H. Dong, C. Gong, F. Sun, and S. He, "Extending the scanning angle of a phased array antenna using a thin radome of curved metasurface," *Phys. Status Solidi RRL* (early access).

[49] E. G. Plaza, S. Loredo, G. León, and F. Las-Heras, "Comparison of different structures for transmitarray cells," *Microw. Opt. Technol. Lett.*, vol. 56, no. 6, pp. 1295–1299, Jun. 2013.

[50] E. G. Plaza, G. León, S. Loredo, and F. Las-Heras, "A simple model for analyzing transmitarray lenses," *IEEE Antennas Propag. Mag.*, vol. 57, no. 2, pp. 131–144, Apr. 2015.

[51] E. G. Plaza, G. Leon, S. Loredo, and F. Las-Heras, "Dual polarized transmitarray lens," in *Proc. Eur. Conf. Antennas Propag. (EuCAP)*, The Hague, The Netherlands, Apr. 6–11, 2014, pp. 2305–2308.

[52] E. G. Plaza, G. León, S. Loredo, A. Arboleya, F. Las-Heras, C. M. S. Álvarez, and M. Rodriguez-Pino, "An ultrathin 2-bit near-field transmitarray lens,". *IEEE Antennas and Wireless Propag. Lett.*, vol. 16, pp. 1784-1787, Mar. 2017.